PHYSICAL REVIEW A **97**, 053813 (2018)

Feedback control of persistent-current oscillation based on the atomic-clock technique

Deshui Yu[1] and Rainer Dumke[1,2,*]
[1]*Centre for Quantum Technologies, National University of Singapore, 3 Science Drive 2, Singapore 117543, Singapore*
[2]*Division of Physics and Applied Physics, Nanyang Technological University, 21 Nanyang Link, Singapore 637371, Singapore*

(Received 7 January 2018; published 11 May 2018)

We propose a scheme of stabilizing the persistent-current Rabi oscillation based on the flux qubit-resonator-atom hybrid structure. The low-Q LC resonator weakly interacts with the flux qubit and maps the persistent-current Rabi oscillation of the flux qubit onto the intraresonator electric field. This oscillating electric field is further coupled to a Rydberg-Rydberg transition of the ^{87}Rb atoms. The Rabi-frequency fluctuation of the flux qubit is deduced from measuring the atomic population via the fluorescence detection and stabilized by feedback controlling the external flux bias. Our numerical simulation indicates that the feedback-control method can efficiently suppress the background fluctuations in the flux qubit, especially in the low-frequency limit. This technique may be extensively applicable to different types of superconducting circuits, paving a way to long-term-coherence superconducting quantum information processing.

DOI: 10.1103/PhysRevA.97.053813

I. INTRODUCTION

Hybridizing superconducting circuits and atoms is a promising idea for realizing quantum information processing, transfer, and storage [1–4]. Numerous structures, including indirect coupling via quantum bus [5], direct magnetic-dipole interface [6], and Rydberg-state-mediated electric-dipole coupling [7,8], have been proposed. These hybrid quantum systems also provide a platform for investigating fundamental principles of ultrastrong interaction between electromagnetic fields and atoms [9–11]. Yet, despite all this, the rapid coherence decay of solid-state devices significantly restricts the practical implementation of these hybrid schemes [12–14]. To our best knowledge, the longest coherence times of state-of-the-art superconducting qubits achieved so far in experiment reach only tens of μs [15].

The atomic-clock technology has been proven as the most efficient tool to preserve the coherence of a local harmonic oscillator [16–18]. Employing the similar measurement to superconducting circuits potentially enhances their energy-relaxation and dephasing times. The decoherence mechanisms of various superconducting qubits have been systematically studied [19–22]. On this basis, in [23] it has been theoretically demonstrated that the frequency fluctuations of a charge-qubit Rabi oscillation can be suppressed via the feedback-control method combined with probing the gate-voltage-bias noise. However, since it is not a direct measurement of the qubit-Rabi-oscillation-frequency fluctuations, the feedback-control efficiency could degrade. Additionally, in [23] the necessary condition, i.e., the efficient superconducting-qubit-atomic-reference coupling, is fulfilled by the direct electric-dipole interaction between the Rydberg atoms and the local electric field from the charge-qubit circuit. However, such a direct interface is extremely challenging in the flux-qubit-atom hybrid because of the weak magnetic-dipole interaction. To prevent these two limitations, it is necessary to establish an approach to directly measure the qubit-Rabi-oscillation-frequency fluctuations and generalize it to other types of superconducting circuits.

In this paper, we explore the application of the feedback-control approach in maintaining the Rabi oscillation of the flux-qubit component in a hybrid structure. In this scheme, a low-Q LC resonator is inductively linked to the flux qubit and maps the persistent-current Rabi oscillation of the flux qubit onto the intraresonator electric field which is further electrically coupled to a Rydberg-Rydberg transition of the ^{87}Rb atoms, resulting in a strong indirect flux-qubit-atomic-reference interface. The projection measurement of the atomic reference enables a direct probing of the Rabi-frequency fluctuations of the persistent current flowing in the flux-qubit loop. Feedback controlling the external flux bias enhances the long-term stability of the flux-qubit Rabi oscillator. Such a superconducting-qubit-resonator-atom stabilization scheme can be generalized to other types of superconducting qubits.

II. FLUX-QUBIT OSCILLATOR

We consider a flux qubit [24] biased by an external magnetic flux Φ_{ex} which is produced by a constant-current source (the open loop in Fig. 1). In the basis of clockwise $|L\rangle$ and counterclockwise $|R\rangle$ persistent-current states, the flux-qubit Hamiltonian (without a drive) in the presence of energy fluctuation is [25,26]

$$H = H_0 - \frac{\hbar\delta\varepsilon}{2}\sigma_z^F, \tag{1}$$

with the dominant part

$$H_0 = -\frac{\hbar\varepsilon}{2}\sigma_z^F - \frac{\hbar\Delta}{2}\sigma_x^F. \tag{2}$$

---

[*] rdumke@ntu.edu.sg

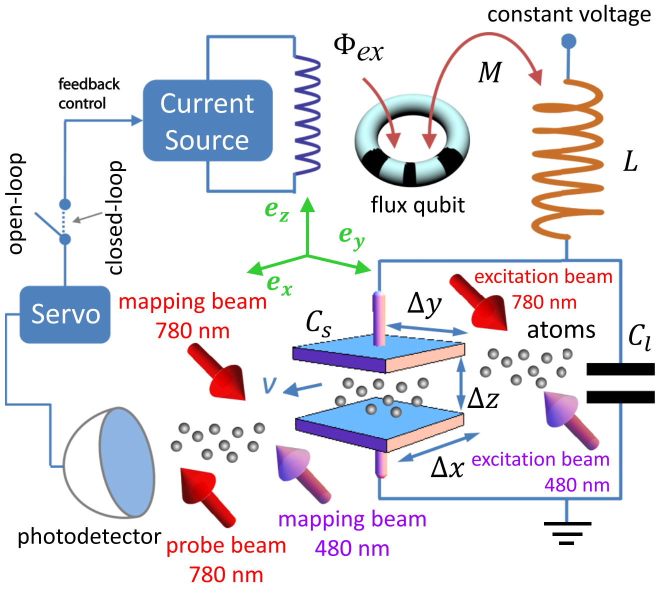

FIG. 1. Schematic diagram of flux-qubit-resonator-atom hybrid. The flux qubit is biased by an external flux Φ_{ex}, generated by a constant-current loop, and is inductively coupled to the low-Q series LC resonator. An ensemble of atoms pass through the capacitor C_s. Before entering C_s, all atoms are excited onto the Rydberg state $|r\rangle \equiv 30\,^2D_{5/2}(m=\frac{5}{2})$ via the two-photon (480 nm and 780 nm) transition. Inside C_s, the Rydberg atoms interact with the intracapacitor electric field. After flying out from C_s, the atoms in $|r\rangle$ are mapped onto the ground state by the 480 nm and 780 nm laser beams. The atomic ground-state population is then measured via a photodetector by the resonance fluorescence at 780 nm. The measurement result is fed back into the constant-current loop via the servo so as to compensate the flux bias Φ_{ex}. The open- and closed-loop systems are controlled by a switch.

$\boldsymbol{\sigma}^F = (\sigma_x^F, \sigma_y^F, \sigma_z^F)$ are the Pauli matrices for the flux qubit. The frequency bias ε between $|L\rangle$ and $|R\rangle$ is written as

$$\varepsilon = \frac{2I_p\Phi_0}{\hbar}\left(\frac{\Phi_{ex}}{\Phi_0} - \frac{1}{2}\right), \tag{3}$$

with the persistent current $I_p = 0.3\ \mu$A [27] and the magnetic flux quantum $\Phi_0 = \frac{\pi\hbar}{e}$. The interstate tunnel rate Δ depends on the specific physical realization of the flux qubit. To facilitate the future implementation of flux-qubit-ultracold-atom hybrids proposed in [6,12], here we set $\Delta = 2\pi\times 6.8$ GHz, which matches the clock transition of the ^{87}Rb atom. $\delta\varepsilon$ denotes the qubit-energy fluctuations caused dominantly by the environmental flux noise. The effects of other noise sources (critical-current and charge noises) are not considered in this work [27,28].

The eigenstates of H_0 are derived as

$$|0\rangle = \cos\frac{\theta}{2}|L\rangle + \sin\frac{\theta}{2}|R\rangle, \tag{4a}$$

$$|1\rangle = -\sin\frac{\theta}{2}|L\rangle + \cos\frac{\theta}{2}|R\rangle, \tag{4b}$$

where θ is determined by $\cos\theta = \frac{\varepsilon}{E_{10}}$ and $\sin\theta = \frac{\Delta}{E_{10}}$ with the frequency spacing $E_{10} = \sqrt{\varepsilon^2 + \Delta^2}$. In the basis of $|0\rangle$ and $|1\rangle$, we have

$$H = \frac{\hbar E_{10}}{2}\Sigma_z^F + \frac{\hbar\delta\varepsilon}{2}\left(\cos\theta\,\Sigma_z^F + \sin\theta\,\Sigma_x^F\right). \tag{5}$$

The Heisenberg equations for the rotated Pauli matrices $\boldsymbol{\Sigma}^F = (\Sigma_x^F, \Sigma_y^F, \Sigma_z^F)$, i.e.,

$$\Sigma_x^F = \cos\theta\,\sigma_x^F - \sin\theta\,\sigma_z^F, \tag{6a}$$

$$\Sigma_y^F = -\sigma_y^F, \tag{6b}$$

$$\Sigma_z^F = -\sin\theta\,\sigma_x^F - \cos\theta\,\sigma_z^F, \tag{6c}$$

are given by

$$\dot{\Sigma}_x^F = -(E_{10} + \delta\varepsilon\,\cos\theta)\Sigma_y^F, \tag{7a}$$

$$\dot{\Sigma}_y^F = (E_{10} + \delta\varepsilon\,\cos\theta)\Sigma_x^F - \delta\varepsilon\,\sin\theta\,\Sigma_z^F, \tag{7b}$$

$$\dot{\Sigma}_z^F = \delta\varepsilon\,\sin\theta\,\Sigma_y^F. \tag{7c}$$

According to the experimental measurements [27,28], the noise spectrum density of $\delta\varepsilon$,

$$S_{\delta\varepsilon}(f) = \int\left[\int \delta\varepsilon(t+\tau)\delta\varepsilon(t)dt\right]e^{-i2\pi f\tau}d\tau, \tag{8}$$

exhibits two distinct regions: the $1/f$ type

$$S_{\delta\varepsilon}(f) = \left(\frac{2I_p\Phi_0}{\hbar}\right)^2 \frac{A_\Phi}{(2\pi f)^{0.9}} \tag{9}$$

for the noise frequency $2\pi f \ll \Delta$ and the ohmic dissipation

$$S_{\delta\varepsilon}(f) = \alpha(2\pi f) \tag{10}$$

for $2\pi f \sim \Delta$.

The quantum behavior of the flux qubit can be simulated by solving Eq. (7), where $\delta\varepsilon$ is numerically generated based on the typical values of $A_\Phi = 5\times 10^{-12}$ [28] and $\alpha = 10^{-5}$ [29]. The energy-relaxation T_1 and dephasing T_2 times of the flux qubit are extracted by the decay of $|1\rangle$ and performing spin echo [Fig. 2(a)]. To verify the validity of our simulation method, we compare the numerical results with the analytical formulas derived from Fermi's golden rule [28–30],

$$T_1^{-1} = \pi\alpha E_{10}\sin^2\theta, \tag{11a}$$

$$T_2^{-1} = \frac{1}{2}T_1^{-1} + \left(\frac{2I_p\Phi_0}{\hbar}\right)\sqrt{A_\Phi \ln 2}\cos\theta. \tag{11b}$$

As shown in Fig. 2(b), they are well matched. T_2 strongly depends on the flux bias Φ_{ex}, while T_1 is almost unchanged. At the optimal bias condition $\Phi_{ex} = 2\Phi_0$ we obtain $T_2 = 2T_1$.

We focus on the flux-qubit Rabi oscillation between $|L\rangle$ and $|R\rangle$. Within the range of Φ_{ex} interested in this work [Fig. 2(b)], we have $(\frac{\varepsilon}{\Delta})^2 \ll 1$. For an ideal system with $\delta\varepsilon = 0$, the persistent-current-flow direction switches alternately clockwise and counterclockwise, i.e., $\langle\sigma_z^F(t)\rangle \simeq \cos E_{10}t$. This may be viewed as a local oscillator with the oscillation frequency of $\omega_{\rm os} = E_{10}$. However, the nonzero $\delta\varepsilon$ disturbs $\omega_{\rm os}$ around E_{10}, leading to the fluctuation $\delta\omega_{\rm os} = \omega_{\rm os} - E_{10}$, which gives rise to the limited $T_{1,2}$. As in atomic clocks, here we employ the Allan deviation $\sigma_{\omega_{\rm os}}^A(\tau)$ to measure the stability of the oscillation (Rabi) frequency $\omega_{\rm os}$ within an average time τ [31]. As illustrated in Fig. 2(c), $\sigma_{\omega_{\rm os}}^A(\tau)$ for different Φ_{ex} are nearly

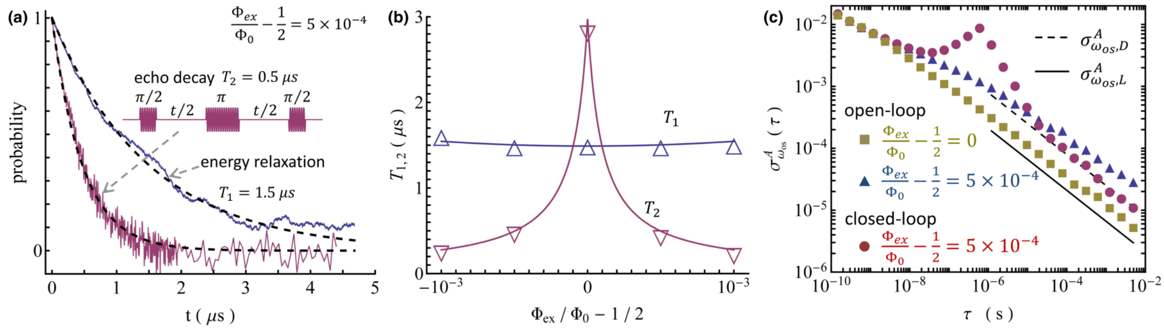

FIG. 2. (a) Numerical simulation of energy relaxation and echo decay of flux qubit with $\frac{\Phi_{ex}}{\Phi_0}-\frac{1}{2}=5\times10^{-4}$ and the initial state $|1\rangle$. (b) Analytical (solid lines) and numerical (△ and ▽) results of energy-relaxation T_1 and dephasing T_2 times as a function of the external flux bias Φ_{ex}. (c) Allan deviation $\sigma_{\omega_{os}}(\tau)$ of Rabi oscillator with different Φ_{ex}, where ■ and ▲ correspond to the open-loop oscillations with $\frac{\Phi_{ex}}{\Phi_0}-\frac{1}{2}=0$ and 5×10^{-4}, while • denotes the feedback-control operation with $\frac{\Phi_{ex}}{\Phi_0}-\frac{1}{2}=5\times10^{-4}$.

the same for $\tau < 1$ ns, corresponding to the fact that T_1 depends less on Φ_{ex}. The $1/f$ component in $\delta\varepsilon$ mainly affects the relatively long-term ($\tau \gg 1$ ns) stability of $\omega_{\rm os}$, resulting in the strong decrease of T_2 for Φ_{ex} away from the optimal point. In the following, we set $\frac{\Phi_{ex}}{\Phi_0}-\frac{1}{2}=5\times10^{-4}$, where $T_1 = 1.5\ \mu$s and $T_2 = 0.5\ \mu$s. Stabilizing $\omega_{\rm os}$ is equivalent to suppress $\delta\varepsilon$, which may potentially enhance $T_{1,2}$.

III. FREQUENCY DISCRIMINATION

We utilize the flux-qubit-resonator-atom hybrid platform established in [3] to discriminate against the fluctuation $\delta\omega_{\rm os}$ of the oscillation (Rabi) frequency $\omega_{\rm os}$. As depicted in Fig. 1, a low-Q series LC resonator, which is biased by a constant voltage source, is weakly coupled to the flux qubit with a mutual inductance of $M = 3$ pH [32]. The resonator's capacitor $C = 0.1$ pF comprises of a large C_l and a small C_s connected in parallel, where $C_s = 4$ fF is formed by a pair of identical parallel plates with the area of $\Delta x\times\Delta y = 0.2\times0.2\ \text{mm}^2$ and the interplate distance of $\Delta z = 0.1$ mm. The resonator frequency $\omega_{LC} = \frac{1}{\sqrt{LC}}$ is set nearly resonant to $\omega_{\rm os}$ with a detuning

$$\begin{aligned}\delta_f &= \omega_{LC} - \omega_{\rm os}\\ &= \delta_{f,0} + \delta\omega_{\rm os},\end{aligned}\tag{12}$$

where we have defined the constant detuning

$$\delta_{f,0} = \omega_{LC} - E_{10},\tag{13}$$

resulting in the inductance $L \approx 5$ nH [33]. We assume that the constant voltage source does not introduce any extra noises.

An ensemble of ^{87}Rb Rydberg atoms (number of n_{at}) fly through C_s in the x direction at the same velocity v. Within C_s, the atoms interact with the nearly homogeneously distributed intracapacitor electric field. This z-direction electric field contains two components: the static $\mathcal{E}_0$, which is produced by the constant voltage bias and tunes the energy spectrum of the atom, and the oscillating $\mathcal{E}$, whose amplitude depends on the detuning δ_f. Figure 3(a) displays the dc Stark map of the Rydberg atom around $|r\rangle \equiv 30^2D_{5/2}(m=\frac{5}{2})$. We focus on two adiabatic energy curves which start respectively from $|r\rangle$ and a manifold state composed of a set of $|n=20, l\leqslant 3, j = l\pm\frac{1}{2}, m=\frac{5}{2}\rangle$ states at the zero field. An energy-level avoided crossing (frequency gap $2\pi\times0.6$ GHz) occurs between two curves at the static electric field of 101.3 V/cm [Fig. 3(b)].

We set $\mathcal{E}_0 = 98.8$ V/cm, where the frequency spacing between two corresponding adiabatic eigenstates (labeled as $|e\rangle$ and $|g\rangle$) is equal to E_{10}. Since other adiabatic states are far apart from $|e\rangle$ and $|g\rangle$, the Rydberg atom may be viewed as a two-level system. The radius of the Rydberg atom is 65 nm [34] and the zero-kelvin lifetime is 25 μs [35]. The large atom-surface separation (50 μm) ensures that the stray fields from the superconducting chip hardly influence the Rydberg states [36]. For $n_{at} = 200$, the average separation among atoms is 15 μm, large enough to suppress the interatomic interactions. Moreover, due to $C_l \gg C_s$ and the large geometric size of C_s, the Rydberg atoms hardly affect the LC-resonator frequency ω_0.

All atoms, before entering C_s, are prepared in $|r\rangle$ via the two-photon $5\,^2S_{1/2}(m=\frac{1}{2}) - 5\,^2P_{3/2}(m=\frac{3}{2}) - |r\rangle$ excitation by using 780 nm and 480 nm laser lights (Fig. 1). When approaching C_s, the atomic state adiabatically follows the corresponding energy curve due to the static fringe field [11]. The oscillating $\mathcal{E}$ field couples to the Rydberg-Rydberg $|e\rangle - |g\rangle$ transition for a time duration of $t_{\rm int} = \Delta x/v$. The atomic $|e\rangle - |g\rangle$ transition rate strongly relies on the flux-qubit-resonator detuning δ_f. As the atoms fly away from C_s, the component in $|e\rangle$ adiabatically evolves back to $|r\rangle$. Then, the atoms in $|r\rangle$ are completely mapped into the ground

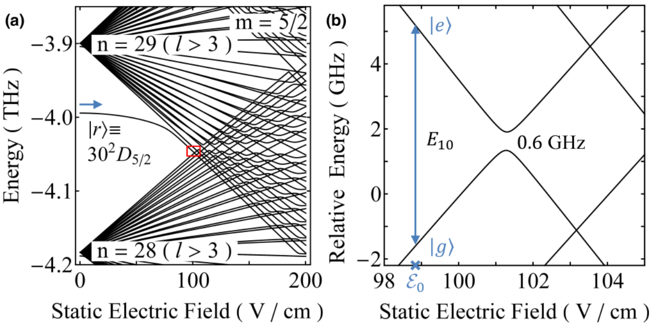

FIG. 3. (a) dc Stark map of ^{87}Rb around $|r\rangle \equiv 30\,^2D_{5/2}(m=\frac{5}{2})$. The detail in the rectangle is displayed in (b), where the energy is relative to the value of 4.05 THz. At $\mathcal{E}_0 = 98.8$ V/cm, the frequency spacing between adiabatic $|e\rangle$ and $|g\rangle$ eigenstates is equal to E_{10}.

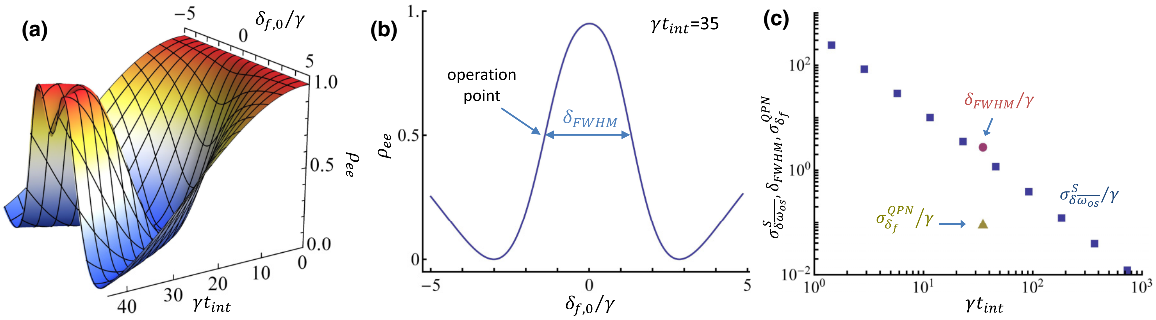

FIG. 4. (a) Probability ρ_{ee} as a function of the constant flux-qubit-resonator detuning $\delta_{f,0}$ and the atom-resonator-interaction time t_{int}. (b) Frequency-discrimination curve, ρ_{ee} vs $\delta_{f,0}$, at $\gamma t_{\text{int}} = 35$. (c) Standard deviation $\sigma^S_{\delta\overline{\omega_{\text{os}}}}$ of the average fluctuations $\delta\overline{\omega_{\text{os}}}$ within t_{int}. The projection-noise-induced uncertainty $\sigma^{QPN}_{\delta_f}$ and the full width at half maximum δ_{FWHM} of the frequency-discrimination curve of (b) are also inserted in (c).

$5\,^2S_{1/2}(m = \frac{1}{2})$ state at a rapid rate (∼ns [37]) via the two-photon transition again. The resulting atomic ground-state population is measured by the fluorescence method based on the $5\,^2S_{1/2}(m = \frac{1}{2}) - 5\,^2P_{3/2}(m = \frac{3}{2})$ transition whose decay rate is $\gamma = 2\pi \times 6.1$ MHz. From the number n_{ph} of fluorescence photons collected by a photodetector during a time length of t_d, the fluctuation $\delta\omega_{\text{os}}$ in the flux-qubit Rabi-oscillation frequency ω_{os} may be derived. Finally, the measured result is fed back into the current source, which produces the flux bias Φ_{ex}, via the servo to tune Φ_{ex} so as to compensate $\delta\omega_{\text{os}}$ (Fig. 1).

Next, we derive the frequency-discrimination curve. The Hamiltonian describing the interface between the Rydberg atoms and the oscillating $\mathcal{E}$ is expressed as

$$\tilde{H} = \frac{\hbar\omega_{eg}}{2}\sigma_z^A + \hbar\Omega\sigma_x^A, \tag{14}$$

where $\sigma_x^A = |e\rangle\langle g| + |g\rangle\langle e|$ and $\sigma_z^A = |e\rangle\langle e| - |g\rangle\langle g|$ are the Pauli matrices for the atoms and the Rabi frequency is defined as $\Omega = -d_0\mathcal{E}/\hbar$ with $d_0 \sim 700ea_0$ [8,38]. The equations of motion of atomic density matrix elements $\rho_{\mu\nu} = \langle\mu|\rho|\nu\rangle$ with $\mu,\nu = e,g$ are derived as

$$\dot{\rho}_{ee} = i\Omega^*\rho_{eg} - i\Omega\rho_{eg}^*, \tag{15a}$$

$$\dot{\rho}_{eg} = -iE_{10}\rho_{eg} + i\Omega^*(2\rho_{ee} - 1). \tag{15b}$$

ρ_{ee} denotes the probability of the atoms being in $|e\rangle$ and ρ_{eg} corresponds to the complex atomic polarizability.

On the other hand, Kirchoff's laws lead to the wave equation for the oscillating electric $\mathcal{E}$ field

$$\ddot{\mathcal{E}} + \kappa\dot{\mathcal{E}} + \omega_{LC}^2\mathcal{E} = -\frac{C_s}{C}\frac{\ddot{\mathcal{P}}}{\varepsilon_0} + \omega_{LC}^2\frac{MI_p}{\Delta z}\dot{\sigma}_z^F, \tag{16}$$

where $\mathcal{P} = \frac{n_{at}d_0}{V_{\text{eff}}}(\rho_{eg} + \rho_{eg}^*)$ is the polarization density of the atoms and V_{eff} is the effective resonator-mode volume. In the limits of $C \gg C_s$ (due to $C_l \gg C_s$) and $V_{\text{eff}} \gg \Delta x\Delta y\Delta z$, the atoms hardly affect $\mathcal{E}$. Thus the first term on the right side of the equal sign in Eq. (16) can be neglected. The second term on the right side of Eq. (16), which originates from the flux-qubit-resonator coupling, plays a role of current driving source. To weaken the resonator filtering effect, the loss rate of the LC resonator is chosen to be $\kappa = 4\gamma$, corresponding to a low Q factor of 300. Moreover, the frequency bias ε of the flux qubit should be rewritten as

$$\varepsilon = \frac{2I_p\Phi_0}{\hbar}\left(\frac{\Phi_{ex}}{\Phi_0} - \frac{1}{2} + \frac{MI}{\Phi_0}\right), \tag{17}$$

where the current I flowing in the resonator is given by

$$I = \Delta zC\frac{d}{dt}\left(\mathcal{E} + \frac{C_s}{C}\frac{\mathcal{P}}{\varepsilon_0}\right). \tag{18}$$

Combining Eqs. (7) and (15), (16), one can simulate the dynamics of the whole hybrid system, i.e., the feedback-controlled Rabi oscillation of the flux qubit. Figure 4(a) depicts the dependence of the probability ρ_{ee} on the constant detuning $\delta_{f,0}$ and the atom-resonator-interaction time t_{int}, where we have set $\delta\omega_{\text{os}} = 0$. It is seen that as t_{int} is increased, ρ_{ee} exhibits the oscillating behavior, i.e., the Rabi oscillation of the atoms. The effect of $\delta_{f,0}$ also merges evidently, i.e., ρ_{ee} for the resonant flux-qubit-resonator coupling ($\delta_{f,0} = 0$) varies much faster than the nonresonant ($\delta_{f,0} \neq 0$) case, for a long enough t_{int}. Indeed, this dependence is caused by the frequency discrimination characteristics of the LC resonator.

For a certain t_{int}, one obtains the one-to-one correspondence between ρ_{ee} and $\delta_{f,0}$ on the negative side of $\delta_{f,0}$. This may be employed to discriminate against the average fluctuation $\delta\overline{\omega_{\text{os}}}$ of the oscillation (Rabi) frequency ω_{os} within t_{int},

$$\delta\overline{\omega_{\text{os}}} = \frac{1}{t_{\text{int}}}\int_0^{t_{\text{int}}}\delta\omega_{\text{os}}(t)dt. \tag{19}$$

The optimal t_{int} relies on the requisite that the standard deviation $\sigma^S_{\delta\overline{\omega_{\text{os}}}}$ of $\delta\overline{\omega_{\text{os}}}$ must satisfy $\sigma^S_{\delta\overline{\omega_{\text{os}}}} < \delta_{FWHM}$, where δ_{FWHM} is the full width at half maximum of the frequency-discrimination curve. Otherwise, $\delta\overline{\omega_{\text{os}}}$ will not be uniquely identified in the frequency-discrimination curve. $\sigma^S_{\delta\overline{\omega_{\text{os}}}}$ should also be larger than the uncertainty $\sigma^{QPN}_{\delta_f} = \frac{\delta_{FWHM}}{2\sqrt{n_{at}}}$ induced by the quantum projection noise [39], which occurs in measuring the atomic population in $|e\rangle$. We set $\gamma t_{\text{int}} = 35$, corresponding to the atomic velocity of $v = 180$ m/s. The corresponding frequency-discrimination curve is plotted in Fig. 4(b), where the stabilization point is commonly chosen at the highest-gradient position, $\delta_{f,0} = -\frac{\delta_{FWHM}}{2}$. Figure 4(c) shows the comparison among $\delta\overline{\omega_{\text{os}}}$, δ_{FWHM}, and $\sigma^{QPN}_{\delta_f}$.

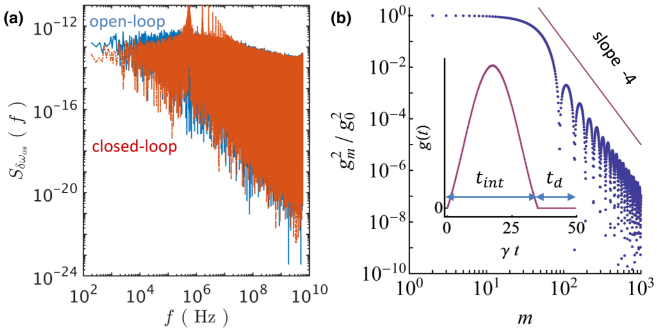

FIG. 5. (a) Power spectral density $S_{\delta\omega_{\text{os}}}(f)$ of the fluctuations $\delta\omega_{\text{os}}$ of open- and closed-loop systems. (b) Spectrum of $g(t)/g_0$. Inset: sensitivity function $g(t)$ within a feedback cycle.

IV. CLOCK OPERATION

Based on the obtained frequency-discrimination curve [Fig. 4(b)], one can derive the average fluctuation $\delta\overline{\omega_{\text{os}}}$ from the atomic-population measurement, which is disturbed by the unavoidable quantum projection noise, via the fluorescence detection (Fig. 1). Another fundamental noise occurring in the population measurement is the photon shot noise arising from the particlelike nature of light [40]. The corresponding signal-to-noise ratio is given by $\frac{1}{\sqrt{n_{\text{ph}}}}$ [41]. To suppress the photon shot noise, we set $\gamma t_d = 15$, resulting in $n_{\text{ph}} = 15$ for an efficient collection of fluorescence photons.

From the derived $\delta\overline{\omega_{\text{os}}}$, one can further calculate the average value $\delta\bar{\varepsilon}$ of the energy-spacing fluctuation $\delta\varepsilon$ within t_{int}, i.e.,

$$\delta\bar{\varepsilon} = \sqrt{(E_{10} + \delta\overline{\omega_{\text{os}}})^2 - \Delta^2} - \varepsilon. \tag{20}$$

$\delta\bar{\varepsilon}$ may be compensated by tuning ε via feedback controlling Φ_{ex}, which is produced by a constant current source, at the end of the fluorescence-photon collection (the closed loop in Fig. 1). Repeating the whole process leads to a stabilized persistent-current Rabi oscillation of the flux qubit. The feedback-control cycle $T_c = 1.3\ \mu$s consists of an atom-resonator-interaction duration t_{int} and a dead-time period t_d for collecting fluorescence photons. Suppressing T_c requires a larger dipole moment d_0, i.e., higher Rydberg states, and a faster decay rate γ. It should be noted that since t_d occupies over one-third of T_c, the feedback-control efficiency is reduced.

Combining Eqs. (7) and (15), (16), we numerically perform the clock running, where ε in Eq. (7) is corrected by $\delta\bar{\varepsilon}$ every T_c. In Fig. 5(a), we compare the spectral density of the fluctuation $\delta\omega_{\text{os}}$ of the oscillation (Rabi) frequency ω_{os},

$$S_{\delta\omega_{\text{os}}}(f) = \int \left[\int \delta\omega_{\text{os}}(t+\tau)\delta\omega_{\text{os}}(t)dt \right] e^{-i2\pi f\tau} d\tau, \tag{21}$$

for both open- and closed-loop systems. It is seen that the feedback control barely affects $S_{\delta\omega_{\text{os}}}(f)$ for $f > T_c^{-1} \sim 1$ MHz while suppressing the fluctuations in the closed-loop system in the low-f ($f < T_c^{-1}$) regime. The corresponding $\sigma^A_{\omega_{\text{os}}}(\tau)$ of the clock operation is displayed in Fig. 2(c). As one can see, the closed-loop $\sigma^A_{\omega_{\text{os}}}(\tau)$ is lower than that of the open-loop system after $\tau > T_c$, indicating the improvement of frequency stability of persistent-current oscillator. However, we should note that the energy-relaxation time T_1 of the closed-loop flux qubit is not extended since T_c is similar to the free-running T_1.

According to [42], the stability of ω_{os} is limited, in principle, by

$$\sigma^A_{\omega_{\text{os}},L}(\tau) = \frac{1}{Q}\sqrt{\frac{T_c}{\tau}}\left(\frac{1}{n_{at}} + \frac{1}{n_{at}n_{\text{ph}}}\right)^{1/2} = \frac{2.1\times 10^{-7}}{\sqrt{\tau}}, \tag{22}$$

where $Q = \frac{E_{10}}{\delta_{FWHM}} = 400$ denotes the Q factor of the frequency-discrimination curve, and the first term in the brackets is the quantum projection noise, while the second term corresponds to the photon shot noise occurring in the fluorescence detection. However, as demonstrated in Fig. 2(c), $\sigma^A_{\omega_{\text{os}},L}(\tau)$ is much lower than the closed-loop $\sigma^A_{\omega_{\text{os}}}(\tau)$. This is because the Dick effect, induced by the interrogation frequency noise and nonzero dead time in the feedback cycle, strongly degrades the oscillator's stability [43]. Following [44], the Dick-effect-limited Allan deviation is expressed as

$$\sigma^A_{\omega_{\text{os}},D}(\tau) = \left[\frac{1}{\tau}\sum_{m=1}^{\infty}\frac{g_m^2}{g_0^2}S_{\delta\omega_{\text{os}}}\left(\frac{m}{T_c}\right)\right]^{1/2} = \frac{7.9\times 10^{-7}}{\sqrt{\tau}}, \tag{23}$$

where the relevant coefficients are defined as $g_0 = \frac{1}{T_c}\int_0^{T_c} g(t)dt$, $g_m^2 = g_{c,m}^2 + g_{s,m}^2$, $g_{c,m} = \frac{1}{T_c}\int_0^{T_c} g(t)\cos\frac{2\pi mt}{T_c}dt$, and $g_{s,m} = \frac{1}{T_c}\int_0^{T_c} g(t)\sin\frac{2\pi mt}{T_c}dt$. The sensitivity function $g(t)$ to the frequency fluctuations of the flux-qubit Rabi oscillation, which may be assumed to have the form $I_p\cos E_{10}t$, is defined as

$$g(t) = 2\lim_{\Delta\phi\to 0}\frac{\delta\rho_{ee}(t)}{\Delta\phi}. \tag{24}$$

$\delta\rho_{ee}(t)$ denotes the change of the probability of the atoms being in $|e\rangle$, caused by an infinitesimally small phase step $\Delta\phi$ of the oscillator signal, i.e., $\cos E_{10}t \to \cos(E_{10}t + \Delta\phi)$, arising at time t.

Figure 5(b) depicts the numerical result of $g(t)$, which is similar to that of the common Rabi interrogation in optical lattice clocks [45], and (g_m^2/g_0^2) vs m. It is seen that the low-frequency fluctuations of ω_{os} primarily affect $\sigma^A_{\omega_{\text{os}},D}(\tau)$. The resulting $\sigma^A_{\omega_{\text{os}},D}(\tau)$ is inserted in Fig. 2(c), which proves that the long-term stability of ω_{os} is limited by the Dick effect. Reducing the dead time t_d may suppress $\sigma^A_{\omega_{\text{os}},D}(\tau)$. However, the shorter t_d leads to the decrease of n_{ph}, which raises $\sigma^A_{\omega_{\text{os}},L}(\tau)$.

V. CONCLUSION

We have investigated the stabilization of a flux-qubit Rabi oscillation by the clock-stability-transfer technique. The system is based on the flux-qubit-resonator-atom hybrid structure, where the periodic persistent-current oscillation of the flux qubit is locked to a microwave Rydberg-Rydberg transition of the ^{87}Rb atom via the resonator serving as a quantum bus. The efficiency of the proposed scheme is restricted mainly by the long cycle time (low-frequency feedback), compared to the decoherence times of the free-running oscillator, and the Dick-effect-induced down-conversion of frequency fluctuations in oscillation. Nevertheless, this low-frequency regime will become a significant challenge in the future qubit engineering.

This superconducting-qubit-resonator-atom hybrid platform may be generalized to other types of superconducting qubits. So far, the coherent superconducting-qubit-resonator coupling has been well demonstrated in experiments [15,32,46]. In contrast, the implementation of superconducting-circuit-atom interface is very limited, despite plenty of relevant theoretical proposals [1–8]. The main challenge is manipulating neutral atoms nearby the cryogenic surface. However, the recent experiments [47–49] show that coupling ultracold (Rydberg) atoms to a superconducting resonator is attainable. Given by the continuing dramatic progress in reducing intrinsic noises in superconducting devices, the development of low-temperature electronics further combined with the clock technology may potentially be widely applied in superconducting quantum information processing, allowing it to be immune to environmental noises [50].

ACKNOWLEDGMENTS

D.Y. would like to thank Hidetoshi Katori for the support of the feedback-control code. This research has been supported by the National Research Foundation Singapore and by the Ministry of Education Singapore Academic Research Fund Tier 2 (Grant No. MOE2015-T2-1-101).

---

[1] Z.-L. Xiang, S. Ashhab, J. Q. You, and F. Nori, Rev. Mod. Phys. **85**, 623 (2013).

[2] D. Yu, M. M. Valado, C. Hufnagel, L. C. Kwek, L. Amico, and R. Dumke, Sci. Rep. **6**, 38356 (2016).

[3] D. Yu, L. C. Kwek, L. Amico, and R. Dumke, Quantum Sci. Technol. **2**, 035005 (2017).

[4] C. Hufnagel, A. Landra, L. C. Chean, D. Yu, and R. Dumke, Proc. SPIE **10358**, 103580D (2017).

[5] D. Petrosyan and M. Fleischhauer, Phys. Rev. Lett. **100**, 170501 (2008).

[6] K. R. Patton and U. R. Fischer, Phys. Rev. A **87**, 052303 (2013).

[7] D. Yu, M. M. Valado, C. Hufnagel, L. C. Kwek, L. Amico, and R. Dumke, Phys. Rev. A **93**, 042329 (2016).

[8] D. Yu, A. Landra, M. M. Valado, C. Hufnagel, L. C. Kwek, L. Amico, and R. Dumke, Phys. Rev. A **94**, 062301 (2016).

[9] T. Niemczyk, F. Deppe, H. Huebl, E. P. Menzel, F. Hocke, M. J. Schwarz, J. J. Garcia-Ripoll, D. Zueco, T. Hümmer, E. Solano, A. Marx, and R. Gross, Nat. Phys. **6**, 772 (2010).

[10] F. Yoshihara, T. Fuse, S. Ashhab, K. Kakuyanagi, S. Saito, and K. Semba, Nat. Phys. **13**, 44 (2017).

[11] D. Yu, L. C. Kwek, L. Amico, and R. Dumke, Phys. Rev. A **95**, 053811 (2017).

[12] J. E. Hoffman, J. A. Grover, Z. Kim, A. K. Wood, J. R. Anderson, A. J. Dragt, M. Hafezi, C. J. Lobb, L. A. Orozco, S. L. Rolston, J. M. Taylor, C. P. Vlahacos, and F. C. Wellstood, Rev. Mex. Fís. S **57**, 1 (2011).

[13] S. Bernon, H. Hattermann, D. Bothner, M. Knufinke, P. Weiss, F. Jessen, D. Cano, M. Kemmler, R. Kleiner, D. Koelle, and J. Fortágh, Nat. Commun. **4**, 2380 (2013).

[14] P. Weiss, M. Knufinke, S. Bernon, D. Bothner, L. Sárkány, C. Zimmermann, R. Kleiner, D. Koelle, J. Fortágh, and H. Hattermann, Phys. Rev. Lett. **114**, 113003 (2015).

[15] C. Wang, Y. Y. Gao, P. Reinhold, R. W. Heeres, N. Ofek, K. Chou, C. Axline, M. Reagor, J. Blumoff, K. M. Sliwa, L. Frunzio, S. M. Girvin, L. Jiang, M. Mirrahimi, M. H. Devoret, and R. J. Schoelkopf, Science **352**, 1087 (2016).

[16] M. Takamoto, F.-L. Hong, R. Higashi, and H. Katori, Nature (London) **435**, 321 (2005).

[17] T. Akatsuka, M. Takamoto, and H. Katori, Nat. Phys. **4**, 954 (2008).

[18] I. Ushijima, M. Takamoto, M. Das, T. Ohkubo, and H. Katori, Nat. Photon. **9**, 185 (2015).

[19] O. Astafiev, Yu. A. Pashkin, Y. Nakamura, T. Yamamoto, and J. S. Tsai, Phys. Rev. Lett. **93**, 267007 (2004).

[20] G. Ithier, E. Collin, P. Joyez, P. J. Meeson, D. Vion, D. Esteve, F. Chiarello, A. Shnirman, Y. Makhlin, J. Schriefl, and G. Schön, Phys. Rev. B **72**, 134519 (2005).

[21] A. Lupaşcu, C. J. P. M. Harmans, and J. E. Mooij, Phys. Rev. B **71**, 184506 (2005).

[22] S. M. Anton, J. S. Birenbaum, S. R. O'Kelley, V. Bolkhovsky, D. A. Braje, G. Fitch, M. Neeley, G. C. Hilton, H.-M. Cho, K. D. Irwin, F. C. Wellstood, W. D. Oliver, A. Shnirman, and J. Clarke, Phys. Rev. Lett. **110**, 147002 (2013).

[23] D. Yu, A. Landra, L. C. Kwek, L. Amico, and R. Dumke, New J. Phys. **20**, 023031 (2018).

[24] J. E. Mooij, T. P. Orlando, L. Levitov, L. Tian, C. H. van der Wal, and S. Lloyd, Science **285**, 1036 (1999).

[25] I. Chiorescu, Y. Nakamura, C. J. P. M. Harmans, and J. E. Mooij, Science **299**, 1869 (2003).

[26] F. Yoshihara, Y. Nakamura, F. Yan, S. Gustavsson, J. Bylander, W. D. Oliver, and J.-S. Tsai, Phys. Rev. B **89**, 020503 (2014).

[27] K. Kakuyanagi, T. Meno, S. Saito, H. Nakano, K. Semba, H. Takayanagi, F. Deppe, and A. Shnirman, Phys. Rev. Lett. **98**, 047004 (2007).

[28] F. Yoshihara, K. Harrabi, A. O. Niskanen, Y. Nakamura, and J. S. Tsai, Phys. Rev. Lett. **97**, 167001 (2006).

[29] Y. Makhlin, G. Schön, and A. Shnirman, Rev. Mod. Phys. **73**, 357 (2001).

[30] Y. Makhlin, G. Schön, and A. Shnirman, in *New Directions in Mesoscopic Physics (Towards Nanoscience)*, edited by R. Fazio, V. F. Gantmakher, and Y. Imry (Kluwer, Dordrecht, 2003), pp. 197–224.

[31] F. Riehle, *Frequency Standards: Basics and Applications* (Wiley, New York, 2004).

[32] I. Chiorescu, P. Bertet, K. Semba, Y. Nakamura, C. J. P. M. Harmans, and J. E. Mooij, Nature (London) **431**, 159 (2004).

[33] M. R. Vissers, J. Hubmayr, M. Sandberg, S. Chaudhuri, C. Bockstiegel, and J. Gao, Appl. Phys. Lett. **107**, 062601 (2015).

[34] R. Löw, H. Weimer, J. Nipper, J. B. Balewski, B. Butscher, H. P. Büchler, and T. Pfau, J. Phys. B **45**, 113001 (2012).

[35] D. B. Branden, T. Juhasz, T. Mahlokozera, C. Vesa, R. O. Wilson, M. Zheng, A. Kortyna, and D. A. Tate, J. Phys. B **43**, 015002 (2012).

[36] J. A. Crosse, S. Å. Ellingsen, K. Clements, S. Y. Buhmann, and S. Scheel, Phys. Rev. A **82**, 010901 (2010).

[37] B. Huber, T. Baluktsian, M. Schlagmüller, A. Kölle, H. Kübler, R. Löw, and T. Pfau, Phys. Rev. Lett. **107**, 243001 (2011).

[38] T. F. Gallagher, *Rydberg Atoms* (Cambridge University Press, New York, 1994).

[39] W. M. Itano, J. C. Bergquist, J. J. Bollinger, J. M. Gilligan, D. J. Heinzen, F. L. Moore, M. G. Raizen, and D. J. Wineland, Phys. Rev. A **47**, 3554 (1993).

[40] C. W. J. Beenakker and M. Patra, Mod. Phys. Lett. B **13**, 337 (1999).

[41] G. C. Bjorklund, M. D. Levenson, W. Lenth, and C. Ortiz, Appl. Phys. B **32**, 145 (1983).

[42] G. Santarelli, Ph. Laurent, P. Lemonde, A. Clairon, A. G. Mann, S. Chang, A. N. Luiten, and C. Salomon, Phys. Rev. Lett. **82**, 4619 (1999).

[43] M. Takamoto, T. Takano, and H. Katori, Nat. Photon. **5**, 288 (2011).

[44] G. Santarelli, C. Audoin, A. Makdissi, P. Laurent, G. J. Dick, and A. Clairon, IEEE Trans. Ultrason. Ferroelectr. Freq. Control **45**, 887 (1998).

[45] A. Al-Masoudi, S. Dörscher, S. Häfner, U. Sterr, and C. Lisdat, Phys. Rev. A **92**, 063814 (2015).

[46] F. Yan, S. Gustavsson, A. Kamal, J. Birenbaum, A. P. Sears, D. Hover, T. J. Gudmundsen, D. Rosenberg, G. Samach, S. Weber, J. L. Yoder, T. P. Orlando, J. Clarke, A. J. Kerman, and W. D. Oliver, Nat. Commun. **7**, 12964 (2016).

[47] T. Thiele, S. Filipp, J. A. Agner, H. Schmutz, J. Deiglmayr, M. Stammeier, P. Allmendinger, F. Merkt, and A. Wallraff, Phys. Rev. A **90**, 013414 (2014).

[48] M. Stammeier, S. Garcia, T. Thiele, J. Deiglmayr, J. A. Agner, H. Schmutz, F. Merkt, and A. Wallraff, Phys. Rev. A **95**, 053855 (2017).

[49] H. Hattermann, D. Bothner, L. Y. Ley, B. Ferdinand, D. Wiedmaier, L. Sárkány, R. Kleiner, D. Koelle, and J. Fortágh, Nat. Commun. **8**, 2254 (2017).

[50] R. Vijay, C. Macklin, D. H. Slichter, S. J. Weber, K. W. Murch, R. Naik, A. N. Korotkov, and I. Siddiqi, Nature (London) **490**, 77 (2012).